



Kinematic Shakedown Analysis for Strain-Hardening Plates with the C^1 Nodal Natural Element Method

Shutao Zhou¹ · Xiaohui Wang¹ · Yatang Ju¹

Received: 18 October 2023 / Revised: 9 March 2024 / Accepted: 14 March 2024
© The Chinese Society of Theoretical and Applied Mechanics 2024

Abstract

This paper proposes a novel numerical solution approach for the kinematic shakedown analysis of strain-hardening thin plates using the C^1 nodal natural element method (C^1 nodal NEM). Based on Koiter's theorem and the von Mises and two-surface yield criteria, a nonlinear mathematical programming formulation is constructed for the kinematic shakedown analysis of strain-hardening thin plates, and the C^1 nodal NEM is adopted for discretization. Additionally, König's theory is used to deal with time integration by treating the generalized plastic strain increment at each load vertex. A direct iterative method is developed to linearize and solve this formulation by modifying the relevant objective function and equality constraints at each iteration. Kinematic shakedown load factors are directly calculated in a monotonically converging manner. Numerical examples validate the accuracy and convergence of the developed method and illustrate the influences of limited and unlimited strain-hardening models on the kinematic shakedown load factors of thin square and circular plates.

Keywords Shakedown analysis · Kinematic theorem · Strain-hardening · Triangular sub-domain stabilized conforming nodal integration · C^1 nodal natural element method

1 Introduction

Thin plate structures are widely used in aerospace, aviation, nuclear energy, shipbuilding and other engineering fields. The precise and reliable computation of the plastic limit-bearing capacity is a very important issue for optimizing the design and safety assessment of thin plate structures under cyclic loading. Compared to traditional linear elastic methods, applying plastic theory to evaluate the bearing capacity of plates not only fully utilizes materials' plastic properties, but also has important theoretical research and practical application value in terms of reducing costs and saving resources. Shakedown analysis is a significant branch of plastic mechanics that provides a direct and effective method for investigating the structural plastic failure load under repeated

loading, without involving the load change history needed in elastic–plastic incremental analysis, and is just connected to the applied external load and structure's material characteristics. Koiter's theorem [1] (kinematic or upper bound theorem) and Melan's theorem [2] (static or lower bound theorem) are two fundamental theories of shakedown analysis, where the kinematically admissible strain field is modified to solve the minimum shakedown load in the former, and the statically admissible residual stress field is optimized to calculate the maximum shakedown load in the latter. The obtained shakedown loads are important parameters that truly reflect the safety margin of structures and have already been used in many design codes and regulations of engineering structures [3].

Up to now, theoretical researches and engineering applications of shakedown analysis have progressed significantly. However, investigations of shakedown analysis for thin plates remain relatively scarce compared to their limit analysis. Theoretical and experimental works have been limited by structural geometry, boundary conditions, loading characteristics, etc., and few achievements have been reported. Notable studies include those by Li et al. [4], Chinh [5, 6], and Yu et al. [7]. With the rapid development of computer technologies and numerical calculation methods, some scholars

✉ Shutao Zhou
zhoushuta-1983@163.com

Xiaohui Wang
wang7274@139.com

Yatang Ju
juyt702@163.com

¹ Beijing Institute of Structure and Environment Engineering,
Beijing 100076, China

have combined mature numerical methods with mathematical programming theorems of shakedown analysis, focused on developing highly efficient optimization algorithms and excellent numerical solution procedures, and published some interesting and remarkable findings. Such works include investigations by Qian and Wang [8], Atkociunas et al. [9], Tran [10], Zheng et al. [11], Blazelevicius et al. [12], and Zhou et al. [13]. However, these studies have not considered the strain-hardening of materials in the shakedown analysis for plates. In fact, many metals and alloys exhibit obvious strain-hardening properties. The shakedown load is sometimes influenced by taking into account the material's strain-hardening effect, and the conservative shakedown load may be obtained when ignoring strain-hardening. Relevant studies include those of Feng and Liu [14], Zhang [15], Xu [16], Simon [17], Ma et al. [18] and Peng et al. [19]. Thus, it is necessary to further develop excellent solution algorithms using accurate and efficient numerical methods and adopt them to study the influence of material's strain-hardening on the shakedown failure loads of plates.

The C^1 natural element method (C^1 NEM) [20] is a unique and fascinating meshless method derived from the natural element method (NEM) [21], which does not require complex matrix operations, only relies on scattered nodal information without nodal mesh data or artificial parameters and has been successfully applied to study the limit and shakedown analyses of thin plates [13, 22, 23]. While the background integration carried out over each Delaunay triangle in the NEM and C^1 NEM provides high accuracy and stability, it also carries the drawbacks of a tremendous amount of computation and inconvenient post-processing, so it is considered to be far from the optimal selection. The stabilized conforming nodal integration (SCNI) with strain smoothing stabilization proposed by Chen et al. [24] effectively overcomes the shortcomings of background integration used in the NEM, and Zhou [25] adopted the nodal NEM [26] with SCNI and Sibson interpolation to obtain accurate upper bound shakedown load multipliers for elastic-perfectly plastic plane structures. Base on the sub-domain stabilized conforming integration (SSCI) developed from SCNI by Wang and Chen [27] for numerical analysis of thin plates, Zhou [28] further proposed the triangular sub-domain stabilized conforming nodal integration (TSNI) scheme and applied the numerical method named C^1 nodal NEM combining advantages of TSNI and C^1 shape functions to study linear elastic analysis of thin plates. The exact numerical results obtained imply that the C^1 nodal NEM is also ideal for kinematic shakedown analysis of strain-hardening thin plates.

This paper proposes an innovative numerical solution method using the C^1 nodal NEM for kinematic shakedown analysis of strain-hardening thin plates. Based on Koiter's theorem and the von Mises and two-surface yield criteria, the associated mathematical programming formulation is

established. The C^1 nodal NEM is used to discretize this formulation, in which the C^1 shape functions are utilized to approximate the trail function of residual displacement increment, and the TSNI scheme is adopted for numerical integration. Time integration involves treating the generalized plastic strain increment at each load vertex, and the nonlinear mathematical programming formulation is linearized and solved directly by revising the objective function and equality constraints iteratively. Ultimately, the accuracy and convergence of the proposed method are demonstrated through numerical examples, and the influences of limited and unlimited strain-hardening models on the kinematic shakedown load factors of thin square and circular plates are illustrated.

2 Kinematic Shakedown Analysis Based on the Two-Surface Yield Criterion

Suppose the studied thin plate described with problem domain $\Omega = S \times h_0$ and displacement boundary Γ_u satisfies the Kirchhoff assumption, where the mid-plane S is set to coincide with the xy -plane and perpendicular to the z -axis, and h_0 stands for the thickness of plate. The classic kinematic shakedown theorem (Koiter's theorem) is expressed as [3, 13, 25]: If there exists a kinematically admissible strain rate cycle that causes the external work rate from imposed loads to exceed the structural plastic dissipation work rate, shakedown does not occur. Accordingly, this paper establishes the following mathematical programming formulation for the kinematic shakedown analysis of strain-hardening plates [13, 28]:

$$s = \min_{\dot{\kappa}^P} \int_0^T \int_{\Omega} D(\dot{\kappa}^P) d\Omega dt \quad (1)$$

$$\int_0^T \int_{\Omega} \mathbf{M}^{eT} \dot{\kappa}^P d\Omega dt = 1 \quad (2)$$

$$\Delta \kappa^P = \int_0^T \dot{\kappa}^P dt = \tilde{\mathbf{B}}(\Delta \mathbf{a}) \quad \text{in } \Omega \quad (3)$$

$$\Delta \mathbf{a} = \int_0^T \dot{\mathbf{a}} dt \quad \text{in } \Omega \quad (4)$$

$$\Delta \mathbf{a} = 0 \quad \text{on } \Gamma_u \quad (5)$$

where s is the kinematic shakedown load factor, T means the loading cycle time, $\dot{\kappa}^P$ represents the vector of generalized plastic strain rate, and $D(\dot{\kappa}^P)$ denotes the plastic dissipation work rate. According to the von Mises yield criterion, and using the two-surface yield criterion to control the yield surface and the movement of its center, $D(\dot{\kappa}^P)$ can be written as [15, 16]:

$$D(\dot{\kappa}^P) = M_P \sqrt{(\dot{\kappa}^P)^T \mathbf{Q}^{-1} \dot{\kappa}^P} + h_P \sqrt{(\Delta \kappa^P)^T \mathbf{Q}^{-1} (\Delta \kappa^P)} \quad (6)$$

In Eqs. (1)–(6), \mathbf{M}^e stands for the vector of virtual generalized pure elastic stress field produced by the independently variable external applied load \mathbf{P} , $\Delta \kappa^P$ and $\Delta \mathbf{a}$, respectively, represent the vectors of generalized plastic strain increment and residual displacement increment generated after one loading cycle during the time interval $t \in [0, T]$, \mathbf{B} denotes the generalized strain–displacement relationship matrix, $\dot{\mathbf{a}} = \{\dot{w} \ \dot{\theta}_x \ \dot{\theta}_y\}^T$ stands for the vector of kinematically admissible displacement velocity field, and \dot{w} , $\dot{\theta}_x = \dot{w}_{,x}$ and $\dot{\theta}_y = \dot{w}_{,y}$, respectively, mean the rate of deflection, and the rates of rotation in the x - and y -directions. $M_P = Y h_0^2/4$ represents the plastic limit bending moment and $h_P = \tilde{h} h_0^2/4$, Y denotes the yield stress of material, \tilde{h} is the material's hardening limit, \mathbf{Q} means a positive-definite symmetric constant matrix, and its inverse matrix is $\mathbf{Q}^{-1} = 2\mathbf{D}/3$, where \mathbf{D} denotes a constant matrix introduced to deal with the plastic incompressibility condition [13, 22].

Equation (1) defines the objective function of this nonlinear minimization problem with time integration, which satisfies the equality constraints named normalization, geometric compatibility, cumulative displacement and displacement boundary conditions in Eqs. (2)–(5), respectively. In Eqs. (1)–(5), the classic assumptions of small deformation, constant elastic modulus and quasi-static loading are adopted.

3 C^1 Nodal Natural Element Method

The C^1 nodal natural element method (C^1 nodal NEM) proposed and named by Zhou [28] is a recent variant of the C^1 NEM [20]. This novel numerical method is also based on the Voronoi diagram and Delaunay triangulation of scattered nodes, adopts the Galerkin method to discretize the global system equation, applies a transformation of the C^1 natural neighbor interpolation to approximate the C^1 shape functions and utilizes the TSCI scheme to perform numerical integration. This paper will firstly present the C^1 shape functions and TSCI scheme.

3.1 C^1 Shape Functions

NP scattered nodes are used to discretize the mid-plane S of the studied thin plate, and n nodes are searched as the natural neighbor nodes of point $\mathbf{x} \in \mathbb{R}^2$ situated on S using the empty circumcircle criterion adopted in the Sibson interpolation [21]. The obtained Sibson shape functions of these n nodes are described as $\phi_1(\mathbf{x}), \phi_2(\mathbf{x}), \dots, \phi_n(\mathbf{x})$, and $\Phi = (\phi_1(\mathbf{x}), \phi_2(\mathbf{x}), \dots, \phi_n(\mathbf{x}))$ is assumed as the natural neighbor coordinate of point \mathbf{x} . Embedding Φ in

the Bernstein–Bézier representation of a cubic simplex to approximate the C^1 shape functions $\Psi(\Phi)$ obtained from the C^1 natural neighbor interpolation, the trial function for deflection $\hat{w}(\Phi)$ of the thin plate can be written in the following matrix form [20]:

$$\hat{w}(\Phi) = \sum_{I=1}^n \Psi_I(\Phi) \mathbf{a}_I = \Psi^T(\Phi) \mathbf{a} \quad (7)$$

with the following defined vectors:

$$\Psi^T(\Phi) = \mathbf{B}^T(\Phi) \mathbf{T} \quad (8)$$

$$\mathbf{a} = \left[w_1 \ \theta_{1x} \ \theta_{1y} \ \dots \ w_n \ \theta_{nx} \ \theta_{ny} \right]^T \quad (9)$$

$$\Psi^T(\Psi) = [\Psi_1(\Phi) \ \Psi_2(\Phi) \ \Psi_3(\Phi) \ \dots \ \Psi_{3n-2}(\Phi) \ \Psi_{3n-1}(\Phi) \ \Psi_{3n}(\Phi)] \quad (10)$$

where $\mathbf{B}(\Phi)$ is the column vector of Bernstein–Bézier basis function. \mathbf{T} stands for the relationship matrix relating the column vector of Bézier ordinates \mathbf{b} and nodal degrees of freedom \mathbf{a} , and $\mathbf{b} = \mathbf{T} \mathbf{a}$. $w_n = w(\mathbf{x}_n)$, $\theta_{nx} = w_{,x}(\mathbf{x}_n)$, and $\theta_{ny} = w_{,y}(\mathbf{x}_n)$, respectively, are the displacement and rotations of node n . $\Psi_{3n-2}(\Phi)$, $\Psi_{3n-1}(\Phi)$ and $\Psi_{3n}(\Phi)$, respectively, represent the C^1 shape functions for nodal displacement w_n , and rotations θ_{nx} and θ_{ny} of node n .

To evaluate the generalized strain–displacement relationship matrix \mathbf{B} in Sect. 3.2, the first-order derivative $\Psi_{,\alpha}^T(\Phi)$ ($\alpha = x, y$) of C^1 shape functions $\Psi^T(\Phi)$ is simply required to be calculated, which can be expressed as [20]:

$$\Psi_{,\alpha}^T(\Phi) = \mathbf{B}_{,\alpha}^T(\Phi) \mathbf{T} \quad (11)$$

where $\mathbf{B}_{,\alpha}(\Phi)$ denotes the first-order derivative of the Bernstein–Bézier basis function $\mathbf{B}(\Phi)$. Further details on calculating and introducing the C^1 shape functions were provided by Sukumar and Moran [20]. The obtained C^1 shape functions possess the Kronecker delta property of nodal function and nodal rotation values, allowing displacement boundary conditions in the C^1 nodal NEM to be treated as easily and precisely as in the finite element method (FEM).

3.2 TSCI Scheme

Based on the principle of Voronoi diagram, the mid-plane S discretized by NP scattered nodes can be divided into a series of domains S_r ($S = \bigcup_{r=1}^{NP} S_r$), with each S_r relating to a node \mathbf{x}_r . To ensure numerical precision and stability for the numerical solution problems of thin plates with high-order partial differential equations, each domain S_r is further divided into RS nonoverlapping triangular sub-domains $S_{r,s}$

($S = \bigcup_{r=1}^{NP} S_r = \bigcup_{r=1}^{NP} \bigcup_{s=1}^{RS} S_{rs}$) around node \mathbf{x}_r , with each S_{rs} relating to a virtual node \mathbf{x}_{rs} . The smoothed generalized strain $\tilde{\kappa}_{ij}(\mathbf{x}_{rs})$ of virtual node \mathbf{x}_{rs} can be written as [27]:

$$\begin{aligned}\tilde{\kappa}_{ij}(\mathbf{x}_{rs}) &= \frac{1}{A_{rs}} \int_{S_{rs}} \kappa_{ij}(\mathbf{x}_{rs}) dS \\ &= \frac{1}{2A_{rs}} \int_{S_{rs}} \{w_{,ij} + w_{,ji}\} dS \\ &= \frac{1}{2A_{rs}} \int_{\Gamma_{rs}} \{w_{,i}n_j + w_{,j}n_i\} d\Gamma\end{aligned}\quad (12)$$

where $i, j = \{x, y\}$; Γ_{rs} and A_{rs} stand for the boundary and area of triangular sub-domain S_{rs} , respectively, and n_i denotes the unit outward normal of boundary Γ_{rs} .

Substituting the trial function of deflection $\hat{w}(\Phi)$ in Eq. (7) into Eq. (12), the vector of smoothed generalized strain $\tilde{\kappa}(\mathbf{x}_{rs})$ can be calculated as:

$$\tilde{\kappa}(\mathbf{x}_{rs}) = \sum_{I=1}^{\bar{n}p} \tilde{\mathbf{B}}_I(\mathbf{x}_{rs}) \mathbf{a}_I \quad (13)$$

$$\tilde{\kappa}(\mathbf{x}_{rs}) = \left[\tilde{\kappa}_x(\mathbf{x}_{rs}) \quad \tilde{\kappa}_y(\mathbf{x}_{rs}) \quad 2\tilde{\kappa}_{xy}(\mathbf{x}_{rs}) \right]^T \quad (14)$$

$\tilde{\mathbf{B}}_I(\mathbf{x}_{rs})$

$$= -\frac{1}{A_{rs}} \int_{\Gamma_{rs}} \begin{bmatrix} \psi_{3I-2,x}(\mathbf{x}_{rs})n_1 & \psi_{3I-1,x}(\mathbf{x}_{rs})n_1 & \psi_{3I,x}(\mathbf{x}_{rs})n_1 \\ \psi_{3I-2,y}(\mathbf{x}_{rs})n_2 & \psi_{3I-1,y}(\mathbf{x}_{rs})n_2 & \psi_{3I,y}(\mathbf{x}_{rs})n_2 \\ \psi_{3I-2,x}(\mathbf{x}_{rs})n_2 + \psi_{3I-2,y}(\mathbf{x}_{rs})n_1 & \psi_{3I-1,x}(\mathbf{x}_{rs})n_2 + \psi_{3I-1,y}(\mathbf{x}_{rs})n_1 & \psi_{3I,x}(\mathbf{x}_{rs})n_2 + \psi_{3I,y}(\mathbf{x}_{rs})n_1 \end{bmatrix} d\Gamma \quad (15)$$

where $\bar{n}p$ is the number of natural neighbor nodes for integral points on the boundary Γ_{rs} of triangular sub-domain S_{rs} . It is important to point out that the C^1 shape functions cannot be directly calculated when integral points are located on the Delaunay triangle boundaries. Zhou [28] proposed a strategy to slightly offset the coordinate of each Voronoi diagram vertex and properly set the offset factor γ to guarantee computational accuracy and overcome C^1 shape function calculation difficulties.

Compared to the C^1 NEM using background integration, the C^1 nodal NEM adopting the TSCI scheme has obvious advantages in the following aspects [28]: (a) In evaluating the generalized strain–displacement relationship matrix $\tilde{\mathbf{B}}_I(\mathbf{x}_{rs})$ in Eq. (15), only the unit outward normals of boundaries and the first-order derivatives of C^1 shape functions are needed, and the second-order derivatives of C^1 shape functions are not required. (b) The TSCI scheme adopted

in the C^1 nodal NEM is beneficial to the construction of generalized plastic strain increment with high precision and good stability for kinematic shakedown analysis of plates. (c) By using the C^1 nodal NEM, the nodal values, such as generalized plastic strain increment and generalized dissipation work rate, can be directly obtained through simple algebraic calculation, eliminating the need to derive these values from the relevant values at integral points with approximation techniques as in the C^1 NEM and FEM [13, 29], and leading to much simpler post-processing of numerical results.

4 Kinematic Shakedown Analysis of Strain-Hardening Plates

4.1 Discretized Formulation

Building upon the above-mentioned fascinating properties and advantages, the C^1 nodal NEM is utilized to discretize the objective function, normalization condition and geometric compatibility in Eqs. (1)–(3). The corresponding discrete expressions are as follows:

$$s = \min_{\dot{\kappa}^p(\mathbf{x}_{rs})} \int_0^T \sum_{r=1}^{NP} \sum_{s=1}^{RS} A_{rs} \left\{ M_P \sqrt{\left[\dot{\kappa}^p(\mathbf{x}_{rs}) \right]^T \mathbf{Q}^{-1} \left[\dot{\kappa}^p(\mathbf{x}_{rs}) \right]} + h_P \sqrt{\left[\Delta \tilde{\kappa}^p(\mathbf{x}_{rs}) \right]^T \mathbf{Q}^{-1} \left[\Delta \tilde{\kappa}^p(\mathbf{x}_{rs}) \right]} \right\} dt \quad (16)$$

$$\int_0^T \sum_{r=1}^{NP} \sum_{s=1}^{RS} A_{rs} \left[\tilde{\mathbf{M}}^e(\mathbf{x}_{rs}) \right]^T \left[\dot{\kappa}^p(\mathbf{x}_{rs}) \right] dt = 1 \quad (17)$$

$$\Delta \tilde{\kappa}(\mathbf{x}_{rs}) = \int_0^T \dot{\kappa}^p(\mathbf{x}_{rs}) dt = \tilde{\mathbf{B}}(\mathbf{x}_{rs}) (\Delta \mathbf{a}) \quad (18)$$

König's theory [30] is used to deal with the time integration in Eqs. (16)–(18). The smoothed generalized plastic

strain increment $\Delta \tilde{\boldsymbol{\kappa}}(\mathbf{x}_{rs})$ produced during one loading cycle is calculated as the sum of smoothed generalized plastic strain sub-increments $\tilde{\boldsymbol{\kappa}}_k^p(\mathbf{x}_{rs})$ generated by load vertices \mathbf{P}_k ($k = 1, 2, \dots, l$), where $l = 2^v$ denotes the total number of load vertices \mathbf{P}_k ($k = 1, 2, \dots, l$), with v being the number of basis loads applied to the structure. Finally, the discrete mathematical programming formulation for kinematic shakedown analysis of strain-hardening plates can be written as:

$$s = \sum_{r=1}^{NP} \sum_{s=1}^{RS} A_{rs} \sum_{k=1}^l M_P \sqrt{[\tilde{\boldsymbol{\kappa}}_k^p(\mathbf{x}_{rs})]^T \mathbf{Q}^{-1} [\tilde{\boldsymbol{\kappa}}_k^p(\mathbf{x}_{rs})]} + \sum_{r=1}^{NP} \sum_{s=1}^{RS} A_{rs} h_P \sqrt{[\Delta \tilde{\boldsymbol{\kappa}}^p(\mathbf{x}_{rs})]^T \mathbf{Q}^{-1} [\Delta \tilde{\boldsymbol{\kappa}}^p(\mathbf{x}_{rs})]} \quad (19)$$

$$\sum_{r=1}^{NP} \sum_{s=1}^{RS} A_{rs} \sum_{k=1}^l [\tilde{\mathbf{M}}_k^e(\mathbf{x}_{rs})]^T [\tilde{\boldsymbol{\kappa}}_k^p(\mathbf{x}_{rs})] = 1 \quad (20)$$

$$\Delta \tilde{\boldsymbol{\kappa}}^p(\mathbf{x}_{rs}) = \sum_{k=1}^l \tilde{\boldsymbol{\kappa}}_k^p(\mathbf{x}_{rs}) = [\tilde{\mathbf{B}}(\mathbf{x}_{rs})] (\Delta \mathbf{a}) \quad \text{in } \Omega \quad (21)$$

$$\Delta \mathbf{a} = 0 \quad \text{on } \Gamma_u \quad (22)$$

4.2 Iterative Algorithm

Using the Lagrange multipliers λ and \mathbf{L}_{rs} to substitute Eqs. (20)–(21) into Eq. (19), respectively, the following improved objective function can be obtained:

$$L(\tilde{\boldsymbol{\kappa}}_k^p(\mathbf{x}_{rs}), \Delta \mathbf{a}, \lambda, \mathbf{L}_{rs}) = \sum_{r=1}^{NP} \sum_{s=1}^{RS} A_{rs} \left\{ \sum_{k=1}^l M_P \sqrt{[\tilde{\boldsymbol{\kappa}}_k^p(\mathbf{x}_{rs})]^T \mathbf{Q}^{-1} [\tilde{\boldsymbol{\kappa}}_k^p(\mathbf{x}_{rs})]} \right\} + \sum_{r=1}^{NP} \sum_{s=1}^{RS} A_{rs} \left\{ h_P \sqrt{(\Delta \mathbf{a})^T [\tilde{\mathbf{B}}(\mathbf{x}_{rs})]^T \mathbf{Q}^{-1} [\tilde{\mathbf{B}}(\mathbf{x}_{rs})] (\Delta \mathbf{a})} \right\} + \lambda \left\{ 1 - \sum_{r=1}^{NP} \sum_{s=1}^{RS} A_{rs} \sum_{k=1}^l [\tilde{\mathbf{M}}_k^e(\mathbf{x}_{rs})]^T [\tilde{\boldsymbol{\kappa}}_k^p(\mathbf{x}_{rs})] \right\} + \sum_{r=1}^{NP} \sum_{s=1}^{RS} \mathbf{L}_{rs}^T \left\{ \sum_{k=1}^l \tilde{\boldsymbol{\kappa}}_k^p(\mathbf{x}_{rs}) - [\tilde{\mathbf{B}}(\mathbf{x}_{rs})] (\Delta \mathbf{a}) \right\} \quad (23)$$

According to the minimization condition of Eq. (23), let $\partial L / \partial \tilde{\boldsymbol{\kappa}}_k^p(\mathbf{x}_{rs}) = \mathbf{0}$, $\partial L / \partial (\Delta \mathbf{a}) = \mathbf{0}$, $\partial L / \partial \lambda = \mathbf{0}$, and $\partial L / \partial \mathbf{L}_{rs} = \mathbf{0}$. The solution expression for the h -th iteration can be constructed as:

$$\frac{A_{rs} M_P}{\mu_k^h(\mathbf{x}_{rs})} \mathbf{Q}^{-1} [\tilde{\boldsymbol{\kappa}}_k^{ph}(\mathbf{x}_{rs})] - \lambda^h A_{rs} [\tilde{\mathbf{M}}_k^e(\mathbf{x}_{rs})] + \mathbf{L}_{rs}^h = 0 \quad (24)$$

$$\sum_{r=1}^{NP} \sum_{s=1}^{RS} \frac{A_{rs} \tilde{h}_P}{\mu^h(\mathbf{x}_{rs})} [\tilde{\mathbf{B}}(\mathbf{x}_{rs})]^T \mathbf{Q}^{-1} [\tilde{\mathbf{B}}(\mathbf{x}_{rs})] (\Delta \mathbf{a})^h - \sum_{r=1}^{NP} \sum_{s=1}^{RS} [\tilde{\mathbf{B}}(\mathbf{x}_{rs})]^T \mathbf{L}_{rs}^h = 0 \quad (25)$$

$$\sum_{r=1}^{NP} \sum_{s=1}^{RS} A_{rs} \sum_{k=1}^l [\tilde{\mathbf{M}}_k^e(\mathbf{x}_{rs})]^T [\tilde{\boldsymbol{\kappa}}_k^{ph}(\mathbf{x}_{rs})] = 1 \quad (26)$$

$$\sum_{k=1}^l \tilde{\boldsymbol{\kappa}}_k^{ph}(\mathbf{x}_{rs}) = [\tilde{\mathbf{B}}(\mathbf{x}_{rs})] (\Delta \mathbf{a})^h \quad (27)$$

with the following defined intermediate variables:

$$\mu_k^h(\mathbf{x}_{rs}) = \sqrt{[\tilde{\boldsymbol{\kappa}}_k^{p(h-1)}(\mathbf{x}_{rs})]^T \mathbf{Q}^{-1} [\tilde{\boldsymbol{\kappa}}_k^{p(h-1)}(\mathbf{x}_{rs})]} \quad (28)$$

$$\mu^h(\mathbf{x}_{rs}) = \sqrt{[(\Delta \mathbf{a})^{h-1}]^T [\tilde{\mathbf{B}}(\mathbf{x}_{rs})]^T \mathbf{Q}^{-1} [\tilde{\mathbf{B}}(\mathbf{x}_{rs})] (\Delta \mathbf{a})^{h-1}} \quad (29)$$

In Eqs. (24)–(27), the vectors of smoothed generalized plastic strain sub-increment $\tilde{\boldsymbol{\kappa}}_k^{p(h-1)}(\mathbf{x}_{rs})$ and residual displacement increment $(\Delta \mathbf{a})^{h-1}$ are obtained at the $(h-1)$ -th iteration with known values. This iterative solution expression forms a series of linear equations about the unknowns of smoothed generalized plastic strain sub-increment $\tilde{\boldsymbol{\kappa}}_k^{ph}(\mathbf{x}_{rs})$, residual displacement increment $(\Delta \mathbf{a})^h$ and Lagrange multipliers λ^h and \mathbf{L}_{rs}^h .

The iterative formula in Eqs. (24)–(27) can be implemented meaningfully and smoothly under the condition that the intermediate variables $\mu_k^h(\mathbf{x}_{rs})$ and $\mu^h(\mathbf{x}_{rs})$ defined in Eqs. (28)–(29) are nonzero in each iteration. Thus, it is necessary to check the values of $\mu_k^h(\mathbf{x}_{rs})$ and $\mu^h(\mathbf{x}_{rs})$ before proceeding with each iteration. In the initial iteration ($h = 0$), the entire thin plate is assumed to be in a fully nonyielding state, with $\hat{\mu}_k^0(\mathbf{x}_{rs}) = \mu_k^0(\mathbf{x}_{rs}) = 1$ and $\hat{\mu}^0(\mathbf{x}_{rs}) = \mu^0(\mathbf{x}_{rs}) = l$ ($k = 1, 2, \dots, l, r = 1, 2, \dots, NP, s = 1, 2, \dots, RS$). For the h -th iteration, the following definitions are adopted:

$$\hat{\mu}_k^h(\mathbf{x}_{rs}) = \begin{cases} \mu_k^h(\mathbf{x}_{rs}), \mu_k^h(\mathbf{x}_{rs}) > \beta_1 \\ \beta_1, \mu_k^h(\mathbf{x}_{rs}) \leq \beta_1 \end{cases} \quad (30)$$

$$\hat{\mu}^h(\mathbf{x}_{rs}) = \begin{cases} \mu^h(\mathbf{x}_{rs}), \mu^h(\mathbf{x}_{rs}) > \beta_2 \\ \beta_2, \mu^h(\mathbf{x}_{rs}) \leq \beta_2 \end{cases} \quad (31)$$

In Eqs. (30)–(31), the positive decimals β_1 and β_2 are significantly smaller than the integer 1 and are typically defined as:

$$\beta_1 = \left(10^{-5} \sim 10^{-8}\right) \times \sum_{k=1}^l \sum_{r=1}^{NP} \sum_{s=1}^{RS} \mu_k^1(\mathbf{x}_{rs}) / (l \times NP \times RS) \quad (32)$$

$$\mu_k^1(\mathbf{x}_{rs}) = \sqrt{\left[\tilde{\mathbf{k}}_k^{\text{p}0}(\mathbf{x}_{rs})\right]^T \mathbf{Q}^{-1} \left[\tilde{\mathbf{k}}_k^{\text{p}0}(\mathbf{x}_{rs})\right]} \quad (33)$$

$$\beta_2 = \left(10^{-5} \sim 10^{-8}\right) \times \sum_{r=1}^{NP} \sum_{s=1}^{RS} \mu^1(\mathbf{x}_{rs}) / (NP \times RS) \quad (34)$$

$$\mu^1(\mathbf{x}_{rs}) = \sqrt{\left[(\Delta \mathbf{a})^0\right]^T \left[\tilde{\mathbf{B}}(\mathbf{x}_{rs})\right]^T \mathbf{Q}^{-1} \left[\tilde{\mathbf{B}}(\mathbf{x}_{rs})\right] (\Delta \mathbf{a})^0} \quad (35)$$

Referring to the series of transformations and eliminations described by Zhou et al. [13, 25], Eqs. (24)–(27) can be further simplified into the following linear equations involving $\tilde{\mathbf{k}}_k^{\text{p}h}(\mathbf{x}_{rs})$, $(\Delta \mathbf{a})^h$, and λ^h :

$$\begin{aligned} & \sum_{r=1}^{NP} \sum_{s=1}^{RS} A_{rs} \left[\tilde{\mathbf{B}}(\mathbf{x}_{rs})\right]^T \left[\hat{\mathbf{E}}^h(\mathbf{x}_{rs})\right] \left[\tilde{\mathbf{B}}(\mathbf{x}_{rs})\right] (\Delta \mathbf{a})^h \\ & = \sum_{r=1}^{NP} \sum_{s=1}^{RS} A_{rs} \lambda^h \left[\tilde{\mathbf{B}}(\mathbf{x}_{rs})\right]^T \left[\hat{\mathbf{A}}^h(\mathbf{x}_{rs})\right] \left[\hat{\mathbf{B}}^h(\mathbf{x}_{rs})\right] \end{aligned} \quad (36)$$

$$\begin{aligned} \tilde{\mathbf{k}}_k^{\text{p}h}(\mathbf{x}_{rs}) & = \left[\tilde{\mathbf{H}}_k^h(\mathbf{x}_{rs})\right]^{-1} \left[\hat{\mathbf{A}}^h(\mathbf{x}_{rs})\right] \left\{ \left[\tilde{\mathbf{B}}(\mathbf{x}_{rs})\right] (\Delta \mathbf{a})^h - \lambda^h \right. \\ & \left. \left\{ \left[\hat{\mathbf{B}}^h(\mathbf{x}_{rs})\right] - \left[\hat{\mathbf{A}}^h(\mathbf{x}_{rs})\right]^{-1} \left[\tilde{\mathbf{M}}_k^e(\mathbf{x}_{rs})\right] \right\} \right\} \end{aligned} \quad (37)$$

$$\sum_{r=1}^{NP} \sum_{s=1}^{RS} A_{rs} \sum_{k=1}^l \left[\tilde{\mathbf{M}}_k^e(\mathbf{x}_{rs})\right]^T \left[\tilde{\mathbf{k}}_k^{\text{p}h}(\mathbf{x}_{rs})\right] = 1 \quad (38)$$

with the intermediate matrices defined as follows:

$$\tilde{\mathbf{H}}_m^h(\mathbf{x}_{rs}) = \frac{M_P}{\hat{\mu}_m^h(\mathbf{x}_{rs})} \mathbf{Q}^{-1} \quad (39)$$

$$\hat{\mathbf{A}}^h(\mathbf{x}_{rs}) = \left\{ \sum_{m=1}^l \left[\tilde{\mathbf{H}}_m^h(\mathbf{x}_{rs})\right]^{-1} \right\}^{-1} \quad (40)$$

$$\begin{aligned} \hat{\mathbf{B}}^h(\mathbf{x}_{rs}) & = \sum_{m=1}^l \left[\tilde{\mathbf{H}}_m^h(\mathbf{x}_{rs})\right]^{-1} \left[\tilde{\mathbf{M}}_m^e(\mathbf{x}_{rs})\right] \\ & = \left\{ \sum_{m=1}^l \left[\tilde{\mathbf{M}}_m^e(\mathbf{x}_{rs})\right]^T \left[\tilde{\mathbf{H}}_m^h(\mathbf{x}_{rs})\right]^{-1} \right\}^T \end{aligned} \quad (41)$$

$$\begin{aligned} \hat{\mathbf{E}}^h(\mathbf{x}_{rs}) & = \frac{\tilde{h}_P}{\hat{\mu}^h(\mathbf{x}_{rs})} \mathbf{Q}^{-1} + \left\{ \sum_{m=1}^l \left[\tilde{\mathbf{H}}_m^h(\mathbf{x}_{rs})\right]^{-1} \right\}^{-1} \\ & = \frac{\tilde{h}_P}{\hat{\mu}^h(\mathbf{x}_{rs})} \mathbf{Q}^{-1} + \hat{\mathbf{A}}^h(\mathbf{x}_{rs}) \end{aligned} \quad (42)$$

To solve Eqs. (36)–(38), we define the residual displacement increment $(\Delta \mathbf{a})^h$ at the h -th iteration as:

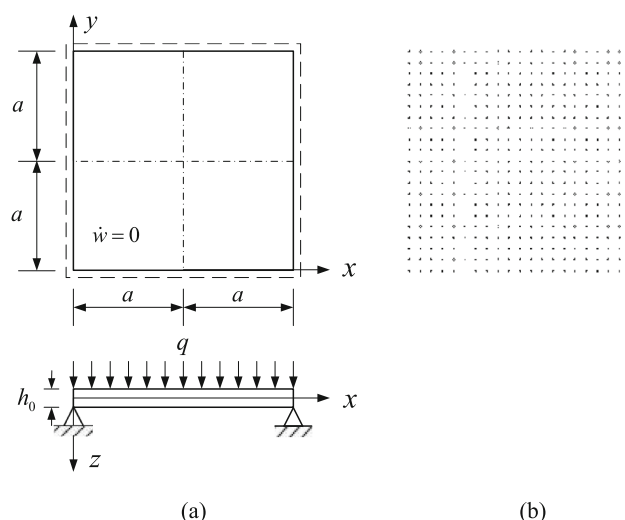


Fig. 1 Model sketch and nodal arrangement of a square plate: **a** simply supported boundary with repeated uniform pressure q ; **b** 441 regular nodes [13]

$$(\Delta \mathbf{a})^h = \lambda^h (\Delta \mathbf{a}_1)^h \quad (43)$$

By substituting Eq. (43) into Eq. (36), we can obtain the following linear control equation:

$$\mathbf{K}^h (\Delta \mathbf{a}_1)^h = \mathbf{F}^h \quad (44)$$

where

$$\mathbf{K}^h = \sum_{r=1}^{NP} \sum_{s=1}^{RS} A_{rs} \left[\tilde{\mathbf{B}}(\mathbf{x}_{rs})\right]^T \left[\hat{\mathbf{E}}^h(\mathbf{x}_{rs})\right] \left[\tilde{\mathbf{B}}(\mathbf{x}_{rs})\right] \quad (45)$$

$$\mathbf{F}^h = \sum_{r=1}^{NP} \sum_{s=1}^{RS} A_{rs} \left[\tilde{\mathbf{B}}(\mathbf{x}_{rs})\right]^T \left[\hat{\mathbf{A}}^h(\mathbf{x}_{rs})\right] \left[\hat{\mathbf{B}}^h(\mathbf{x}_{rs})\right] \quad (46)$$

By introducing the displacement boundary condition of Eq. (22) to modify the matrix \mathbf{K}^h and column vector \mathbf{F}^h in Eqs. (45)–(46), and solving Eq. (44), we can obtain the intermediate vector of residual displacement increment $(\Delta \mathbf{a}_1)^h$. Then, substituting Eq. (43) into Eq. (37), the smoothed generalized plastic strain sub-increment $\tilde{\mathbf{k}}_k^{\text{p}h}(\mathbf{x}_{rs})$ at iteration step h can be calculated as:

$$\tilde{\mathbf{k}}_k^{\text{p}h}(\mathbf{x}_{rs}) = \lambda^h \left[\tilde{\mathbf{H}}_k^h(\mathbf{x}_{rs})\right]^{-1} \left[\hat{\mathbf{C}}^h(\mathbf{x}_{rs}) + \tilde{\mathbf{M}}_k^e(\mathbf{x}_{rs})\right] \quad (47)$$

where

$$\hat{\mathbf{C}}^h(\mathbf{x}_{rs}) = \left[\hat{\mathbf{A}}^h(\mathbf{x}_{rs})\right] \left\{ \left[\tilde{\mathbf{B}}(\mathbf{x}_{rs})\right] (\Delta \mathbf{a}_1)^h - \hat{\mathbf{B}}^h(\mathbf{x}_{rs}) \right\} \quad (48)$$

Table 1 Comparison of kinematic shakedown load factors and computational times for a clamped square plate under different loading cases and material models

Loading cases	Material models	Numerical solutions (M_P/qa^2)		Times (s)	
		C ¹ nodal NEM	C ¹ NEM	C ¹ nodal NEM	C ¹ NEM
$0 \leq q \leq q^{\max}$	$\tilde{h} = 0$	9.773	9.454	863	817
	$\tilde{h} = 0.05Y$	9.780	9.456	757	788
	$\tilde{h} = 0.40Y$	9.782	9.456	726	778
	$\tilde{h} = 0.75Y$	9.782	9.456	–	–
	$\tilde{h} = 1.25Y$	9.782	9.456	–	–
	$\tilde{h} = +\infty$	9.782	9.457	–	–
$-q^{\max} \leq q \leq q^{\max}$	$\tilde{h} = 0$	4.891	4.728	725	778
	$\tilde{h} = 0.05Y$	4.891	4.728	–	–
	$\tilde{h} = 1.25Y$	4.891	4.728	–	–
	$\tilde{h} = +\infty$	4.891	4.728	–	–

Table 2 Comparison of kinematic shakedown load factors and computational times for a simply supported square plate under different loading cases and material models

Loading cases	Material models	Numerical solutions (M_P/qa^2)		Times (s)	
		C ¹ nodal NEM	ACM	C ¹ nodal NEM	ACM
$0 \leq q \leq q^{\max}$	$\tilde{h} = 0$	6.281	6.250 [13]	220	222
	$\tilde{h} = 0.05Y$	6.595	6.562	226	229
	$\tilde{h} = 0.40Y$	8.794	8.750	236	239
	$\tilde{h} = 0.75Y$	9.033	8.972	1055	1009
	$\tilde{h} = 1.25Y$	9.033	8.972	–	–
	$\tilde{h} = +\infty$	9.034	8.973	–	–
$-q^{\max} \leq q \leq q^{\max}$	$\tilde{h} = 0$	4.517	4.486 [13]	1045	1008
	$\tilde{h} = 0.05Y$	4.517	4.486	–	–
	$\tilde{h} = 1.25Y$	4.517	4.486	–	–
	$\tilde{h} = +\infty$	4.517	4.486	–	–

By substituting $\tilde{\boldsymbol{\kappa}}_k^{ph}(\mathbf{x}_{rs})$ in Eq. (47) into Eq. (38), we can derive the Lagrange multiplier λ^h as:

$$\mu^{h+1}(\mathbf{x}_{rs}) = \sqrt{[(\Delta \mathbf{a})^h]^T [\tilde{\mathbf{B}}(\mathbf{x}_{rs})]^T \mathbf{Q}^{-1} [\tilde{\mathbf{B}}(\mathbf{x}_{rs})] (\Delta \mathbf{a})^h} \quad (51)$$

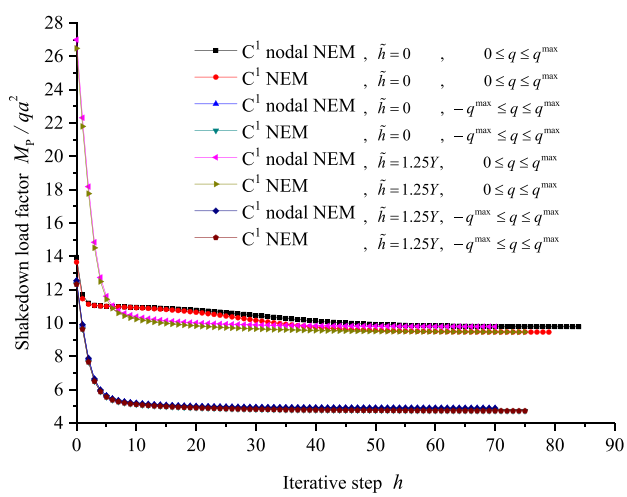
$$\lambda^h = \frac{1}{\sum_{r=1}^{NP} \sum_{s=1}^{RS} A_{rs} \left\{ [\hat{\mathbf{B}}^h(\mathbf{x}_{rs})]^T [\hat{\mathbf{C}}^h(\mathbf{x}_{rs})] + \left\{ \sum_{k=1}^l [\tilde{\mathbf{M}}_k^c(\mathbf{x}_{rs})]^T [\tilde{\mathbf{H}}_k^h(\mathbf{x}_{rs})]^{-1} [\tilde{\mathbf{M}}_k^c(\mathbf{x}_{rs})] \right\} \right\}} \quad (49)$$

Substituting the obtained $(\Delta \mathbf{a}_1)^h$ and λ^h back into Eqs. (43) and (47)–(48), the residual displacement increment $(\Delta \mathbf{a})^h$ and the smoothed generalized plastic strain sub-increment $\tilde{\boldsymbol{\kappa}}_k^{ph}(\mathbf{x}_{rs})$ can be obtained. According to Eqs. (28)–(31), the following intermediate variables can be further calculated as:

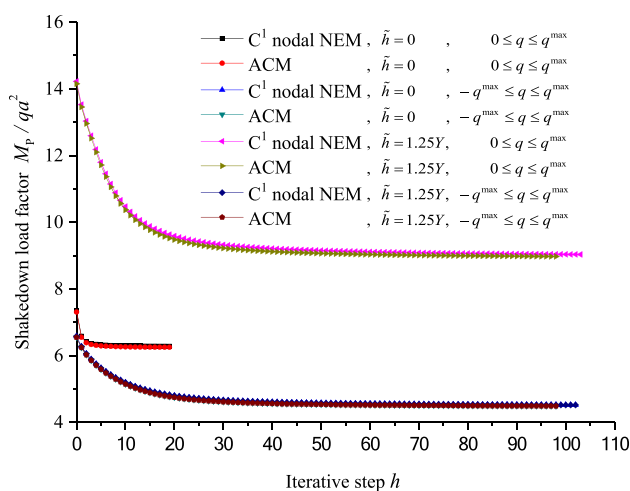
$$\hat{\mu}_k^{h+1}(\mathbf{x}_{rs}) = \begin{cases} \mu_k^{h+1}(\mathbf{x}_{rs}), & \mu_k^{h+1}(\mathbf{x}_{rs}) > \beta_1 \\ \beta_1, & \mu_k^{h+1}(\mathbf{x}_{rs}) \leq \beta_1 \end{cases} \quad (52)$$

$$\mu_k^{h+1}(\mathbf{x}_{rs}) = \sqrt{[\tilde{\boldsymbol{\kappa}}_k^{ph}(\mathbf{x}_{rs})]^T \mathbf{Q}^{-1} [\tilde{\boldsymbol{\kappa}}_k^{ph}(\mathbf{x}_{rs})]} \quad (50)$$

$$\hat{\mu}_k^{h+1}(\mathbf{x}_{rs}) = \begin{cases} \mu_k^{h+1}(\mathbf{x}_{rs}), & \mu_k^{h+1}(\mathbf{x}_{rs}) > \beta_2 \\ \beta_2, & \mu_k^{h+1}(\mathbf{x}_{rs}) \leq \beta_2 \end{cases} \quad (53)$$



(a)



(b)

Fig. 2 Iterative convergence processes of kinematic shakedown load factors for a square plate: **a** clamped; **b** simply supported

Finally, the shakedown load factor s^h at iteration step h can be written as:

$$s^h = \sum_{r=1}^{NP} \sum_{s=1}^{RS} A_{r,s} \left[\sum_{k=1}^l M_P \hat{\mu}_k^{h+1}(\mathbf{x}_{rs}) + h_P \hat{\mu}^{h+1}(\mathbf{x}_{rs}) \right] \quad (54)$$

According to the anticipated computational accuracy, two error tolerances, $vol1$ and $vol2$, are set in the iterative solution program, and the iteration will be terminated when the following convergence conditions are achieved:

$$\left\| (\Delta a)^h - (\Delta a)^{h-1} \right\| / \left\| (\Delta a)^{h-1} \right\| \leq vol1, \quad \left| s^h - s^{h-1} \right| / s^{h-1} \leq vol2 \quad (55)$$

5 Numerical Examples

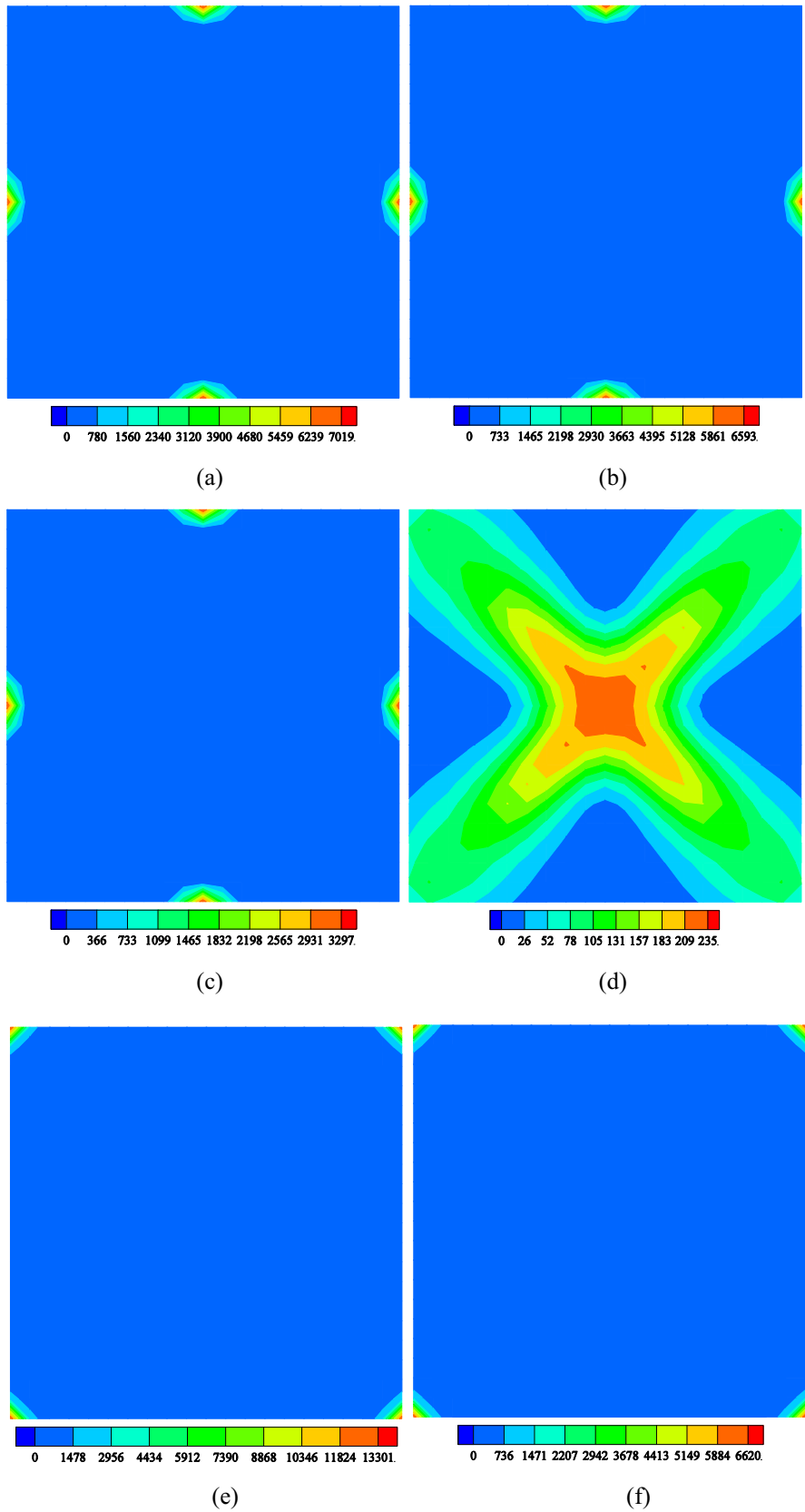
In this section, computer codes are developed based on the iterative algorithm proposed above with C^1 nodal NEM for the kinematic shakedown analysis of thin square and circular plates. The perfectly elasto-plastic ($\tilde{h} = 0$), limited kinematic hardening ($\tilde{h} = 0.05Y, 0.40Y, 0.75Y, 1.25Y$) and unlimited kinematic hardening ($\tilde{h} = +\infty$) material models are considered. The numerical results and computational times obtained using the C^1 NEM and the rectangular non-conforming plate element ACM [31, 32] are also provided for comparison. A two-point quadrature scheme is employed on each boundary line of the triangle sub-domain in the C^1 nodal NEM, a three-point quadrature rule is adopted over each Delaunay triangle in the C^1 NEM, and a 3×3 quadrature rule is used over each finite element in the ACM. The computational times listed below are counted from the same Lenovo computer (Intel(R) Core(TM)2 @ 3.0 GHz). In the numerical calculation, the relevant parameters are set as follows: offset factor $\gamma = 1.0 \times 10^{-5}$ [28], yield stress $Y = 200$ MPa, Young’s modulus $E = 2.1 \times 10^5$ MPa, Poisson’s ratio $\nu = 0.3$ and error tolerances $vol1 = vol2 = 1.0 \times 10^{-4}$. Two loading cases $0 \leq q \leq q^{\max}$ and $-q^{\max} \leq q \leq q^{\max}$ involving repeated uniform transverse pressure q are considered, where q^{\max} denotes a specific maximum magnitude of pressure q , and the reference value of pressure q is set as 1.0 N/m^2 .

5.1 Square Plate

The clamped ($\dot{w} = \partial \dot{w} / \partial x = \partial \dot{w} / \partial y = 0$) and simply supported ($\dot{w} = 0$) thin square plates under the repeated uniform pressure q are studied as the first example. The model sketch is displayed in Fig. 1a, where the length $2a = 1$ m and the thickness $h_0 = 0.01$ m, and the 441 regular nodes displayed in Fig. 1b are adopted for the numerical calculation. The obtained numerical results and the computational times using the C^1 nodal NEM, C^1 NEM and ACM are listed in Tables 1 and 2, respectively.

It can be seen that: (1) In various loading cases and material models, the kinematic shakedown load factors obtained using the C^1 nodal NEM agree well with those from the C^1 NEM and ACM under the same condition, with minimal differences. (2) In the cumulative loading case $0 \leq q \leq q^{\max}$, the limited and unlimited strain-hardening models tend to increase the kinematic shakedown load factors compared to the perfectly elasto-plastic model. For instance, using the C^1 nodal NEM, the load factors for the clamped square plate increase by 0.072% and 0.092% for $\tilde{h} = 0.05Y$ and $\tilde{h} = 0.40Y, 0.75Y, 1.25Y, +\infty$, respectively, and for the simply supported square plate, they increase by 4.999%, 40.010%, 43.815%, and 43.831% for $\tilde{h} = 0.05Y, \tilde{h} = 0.40Y, \tilde{h} = 0.75Y, 1.25Y$, and $\tilde{h} = +\infty$, respectively. (3)

Fig. 3 Distributions of plastic dissipation work rates for a square plate at shakedown limit states (10^6 N m): **a** clamped, $\tilde{h} = 0, 0 \leq q \leq q^{\max}$; **b** clamped, $\tilde{h} = 1.25Y$, $0 \leq q \leq q^{\max}$; **c** clamped, $\tilde{h} = 0$ and $\tilde{h} = 1.25Y$, $-q^{\max} \leq q \leq q^{\max}$; **d** simply supported, $\tilde{h} = 0, 0 \leq q \leq q^{\max}$; **e** simply supported, $\tilde{h} = 1.25Y$, $0 \leq q \leq q^{\max}$; **f** simply supported, $\tilde{h} = 0$ and $\tilde{h} = 1.25Y$, $-q^{\max} \leq q \leq q^{\max}$



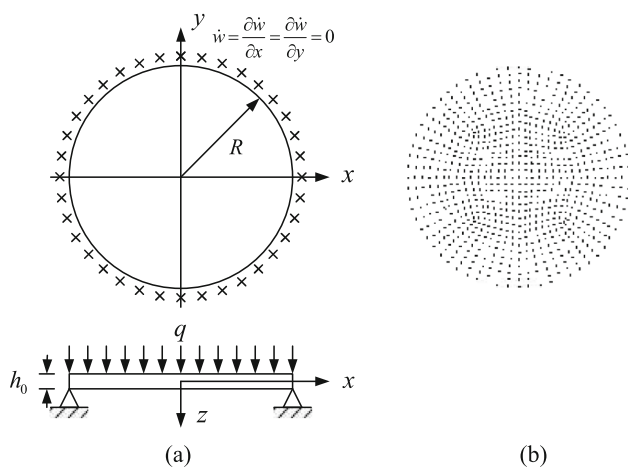


Fig. 4 A clamped circular plate: **a** under uniform pressure q ; **b** 801 nodes [13]

In the alternating loading case $-q^{\max} \leq q \leq q^{\max}$, the load factors obtained for the limited and unlimited kinematic hardening models are equal to those of the perfectly elasto-plastic model under the same condition. (4) In general, the computational times using the C^1 nodal NEM are comparable to those using the C^1 NEM and ACM. As per Zhou et al. [25], the costs of the nodal NEM in shakedown analysis of plane structures are approximately one-ninth to one-third of those of the NEM. However, owing to more triangular sub-domain partitions and numerical integrations on the boundary lines in each triangular sub-domain in the C^1 nodal NEM compared to the nodal NEM, the computational efficiency of the C^1 nodal NEM remains relatively unchanged from that of the C^1 NEM.

Figure 2 displays the iterative convergence processes of kinematic shakedown load factors for some loading cases and material models using the C^1 nodal NEM, C^1 NEM and ACM, which indicates that the proposed iterative algorithm ensures rapid and monotonic convergence of obtained kinematic shakedown load factors to stable minima after 19–103 iterations.

As mentioned in Sect. 3.2, the nodal generalized plastic dissipation work rates in the kinematic shakedown analysis of plates can be directly obtained using the C^1 nodal NEM, and the C^1 nodal NEM offers obvious advantages in numerical result post-processing compared to the C^1 NEM and ACM. Figure 3 shows the distributions of plastic dissipation work rates obtained directly through the C^1 nodal NEM for a thin square plate under different loading cases and material models, which visually illustrates the cumulative and alternating plastic damage modes of the square plate at shakedown limit states.

5.2 Circular Plate

A clamped thin circular plate with the radius $R = 1$ m and the thickness $h_0 = 0.01$ m under the repeated uniform pressure q is examined as the second example. The model sketch and 801 regular nodal arrangement adopted in the numerical calculation are displayed in Fig. 4. By adopting the perfectly elasto-plastic model, Yu et al. [7] employed the unified yield criterion to deduce the analytical solution under the loading case $0 \leq q \leq q^{\max}$, while Zhou et al. [13] utilized the C^1 NEM to solve the numerical results under the loading cases $0 \leq q \leq q^{\max}$ and $-q^{\max} \leq q \leq q^{\max}$. This paper uses the proposed method with the C^1 nodal NEM and C^1 NEM to concurrently determine the kinematic shakedown load factors of this plate, with the results summarized in Table 3.

It shows that: (1) The kinematic shakedown load factor obtained by the C^1 nodal NEM is closer to the analytical solution of Yu et al. [7] than that obtained by the C^1 NEM, which is in good agreement with the conclusion of Zhou [28] that the C^1 nodal NEM has better computational accuracy than the C^1 NEM in the linear elastic analysis of plates. The results obtained by the C^1 nodal NEM and C^1 NEM match well with each other under the same condition, indicating the proposed method in this paper has high computational accuracy. (2) In the cumulative loading case $0 \leq q \leq q^{\max}$, the load factors using the C^1 nodal NEM increase by 5.003%, 22.248%, and 22.371% for $\tilde{h} = 0.05Y$, $\tilde{h} = 0.40Y$, and $\tilde{h} = 0.75Y$, $1.25Y$, $+\infty$, respectively, compared to the perfectly elasto-plastic model. This suggests that the shakedown load obtained may be conservative when the material's strain-hardening effect is disregarded. (3) In the alternating loading case $-q^{\max} \leq q \leq q^{\max}$, the results for limited and unlimited kinematic hardening models align with the perfectly elasto-plastic model.

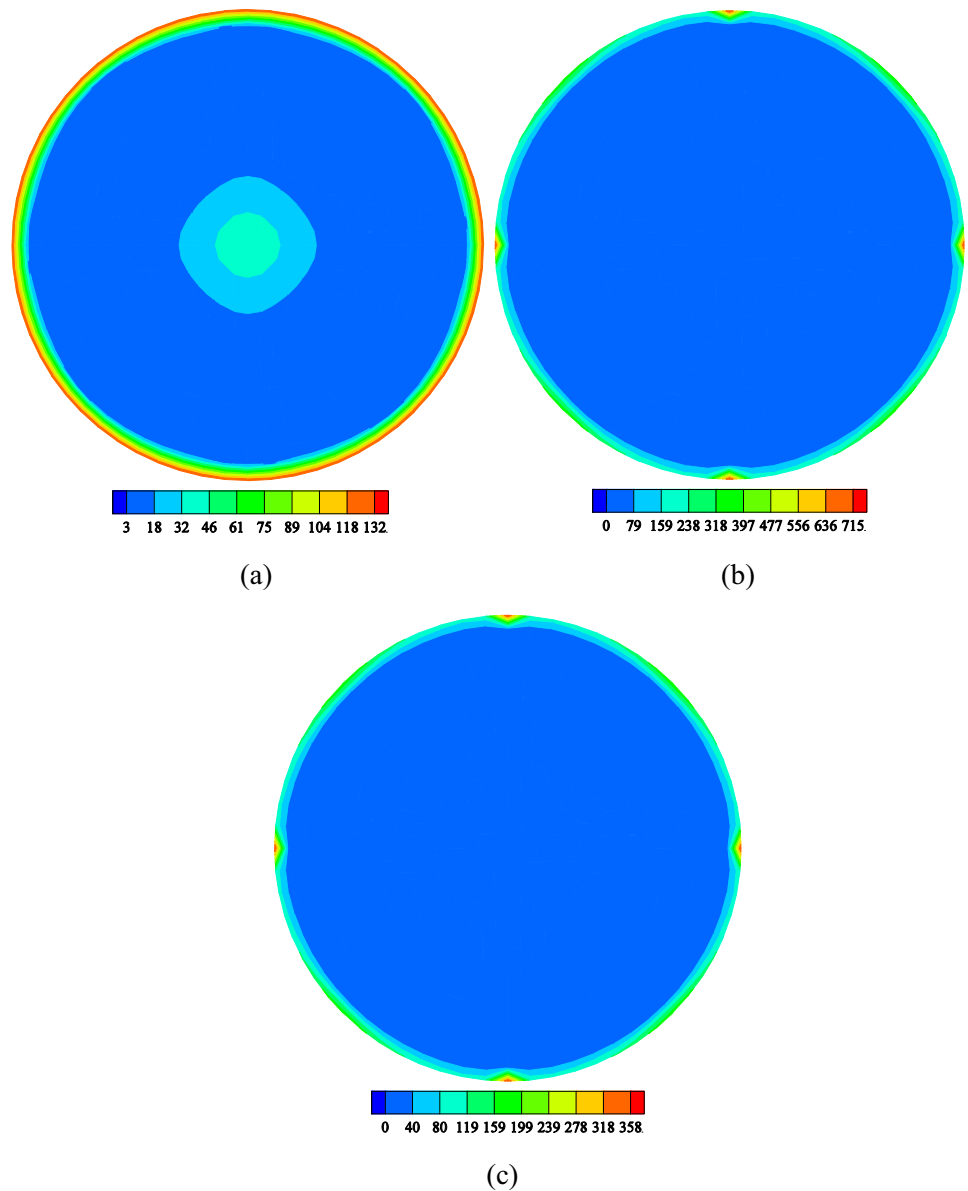
Figure 5 displays the distributions of plastic dissipation work rates obtained using the C^1 nodal NEM, which are symmetrical and reasonable, revealing the plastic failure modes of this clamped circular plate at shakedown limit states.

6 Conclusions

This paper proposes a novel numerical approach using the C^1 nodal NEM to evaluate the kinematic shakedown load factors of strain-hardening plates based on the von Mises and two-surface yield criteria and adopts it to implement kinematic shakedown analysis of thin square and circular plates with perfectly elasto-plastic, limited kinematic hardening and unlimited kinematic hardening material models. The numerical results for kinematic shakedown load factors align closely with theoretical solution and numerical values obtained using the C^1 NEM and ACM. Compared to the perfectly elasto-plastic model, the limited and unlimited

Table 3 Comparison of kinematic shakedown load factors for a clamped circular plate under different loading cases and material models

Loading cases	Material models	Numerical solutions (M_P/qR^2)		
		C^1 nodal NEM	C^1 NEM	Yu et al. [7]
$0 \leq q \leq q^{\max}$	$\tilde{h} = 0$	12.172	12.487 [13]	12.23
	$\tilde{h} = 0.05Y$	12.781	13.110	–
	$\tilde{h} = 0.40Y$	14.880	14.967	–
	$\tilde{h} = 0.75Y$	14.895	14.967	–
	$\tilde{h} = 1.25Y$	14.895	14.967	–
	$\tilde{h} = +\infty$	14.895	14.970	–
$-q^{\max} \leq q \leq q^{\max}$	$\tilde{h} = 0$	7.448	7.483 [13]	–
	$\tilde{h} = 0.05Y$	7.448	7.483	–
	$\tilde{h} = 1.25Y$	7.448	7.483	–
	$\tilde{h} = +\infty$	7.448	7.483	–

Fig. 5 Distributions of plastic dissipation work rates for a clamped circular plate at shakedown limit states (10^6 N m): **a** $\tilde{h} = 0$, $0 \leq q \leq q^{\max}$; **b** $\tilde{h} = 1.25Y$, $0 \leq q \leq q^{\max}$; **c** $\tilde{h} = 0$ and $\tilde{h} = 1.25Y$, $-q^{\max} \leq q \leq q^{\max}$


kinematic hardening models somewhat increase the obtained load factors of thin square and circular plates in cumulative loading cases, but have no impact in alternating loading cases. The distributions of plastic dissipation work rates effectively illustrate the cumulative and alternating plastic failure modes of thin square and circular plates at shakedown limit states. Numerical examples demonstrate the proposed numerical method's benefits of high accuracy, rapid convergence and convenient post-processing capabilities.

Acknowledgements This work is supported by the Chinese Postdoctoral Science Foundation (2013M540934).

References

- Koiter WT. A new general theorem on shakedown of elastic-plastic structures. *Proc Konink Nederl Akad Wetensch B*. 1956;59:24–34.
- Melan E. Zur Plastizität des räumlichen Kontinuums. *Ing-Arch*. 1938;9:115–26.
- Chen G, Liu YH. Numerical theories and engineering methods for structural limit and shakedown analysis. Beijing: Science Press; 2006. (in Chinese).
- Li KY, Liu XS, Xu BY. An experimental shakedown investigation of built-in circular plates. *Chin J Appl Mech*. 1989;6(3):83–8 (in Chinese).
- Chinh PD. Evaluation of shakedown loads for plates. *Int J Mech Sci*. 1997;39(12):1415–22.
- Chinh PD. Plastic collapse of a circular plate under cyclic loads. *Int J Plast*. 2003;19(4):547–59.
- Yu MH, Ma GW, Li JC. Structural plasticity limit, shakedown and dynamic plastic analyses of structures. New York: Springer; 2009.
- Qian LX, Wang ZB. Limit analysis and shakedown analysis of bending plates and rotational shell-method of temperature parameters. *Acta Mech Sin*. 1989;21:118–24 (in Chinese).
- Atkociunas J, Jarmolajeva E, Merkevičute D. Optimal shakedown loading for circular plates. *Struct Multidiscip Optim*. 2004;27(3):178–88.
- Tran TN. A dual algorithm for shakedown analysis of plate bending. *Int J Numer Methods Eng*. 2011;86(7):862–75.
- Zheng H, Peng X, Hu N. Optimal analysis for shakedown of functionally graded (FG) Bree plate with genetic algorithm. *Comput Mater Contin*. 2014;41(1):55–84.
- Blazevičius G, Rimkus L, Merkevičute D, Atkociunas J. Shakedown analysis of circular plates using a yield criterion of the mean. *Struct Multidiscip Optim*. 2017;55:25–36.
- Zhou ST, Liu YH, Ma BJ, Hou CT, Ju YT, Wu B, Rong KL. Upper bound shakedown analysis of plates utilizing the C^1 natural element method. *Acta Mech Solida Sin*. 2021;34(2):221–36.
- Feng XQ, Liu XS. Factors influencing shakedown of elastoplastic structures. *Adv Mech*. 1993;23(2):214–22 (in Chinese).
- Zhang YG. An iteration algorithm for kinematic shakedown analysis. *Comput Methods Appl Mech Eng*. 1995;127(1–4):217–26.
- Xu ZF. Plastic limit and shakedown analysis for curved pipe structures. Beijing: Tsinghua University; 2000. (in Chinese).
- Simon JW. Direct evaluation of the limit states of engineering structures exhibiting limited, nonlinear kinematical hardening. *Int J Plast*. 2013;42:141–67.
- Ma Z, Chen H, Liu Y, Xuan FZ. A direct approach to the evaluation of structural shakedown limit considering limited kinematic hardening and non-isothermal effect. *Eur J Mech A Solids*. 2020;79:103877.
- Peng H, Liu Y, Chen H, Zhang ZM. Shakedown analysis of bounded kinematic hardening engineering structures under complex cyclic loads: theoretical aspects and a direct approach. *Eng Struct*. 2022;256:114034.
- Sukumar N, Moran B. C-1 natural neighbor interpolant for partial differential equations. *Numer Methods Partial Differ Equ*. 1999;15(4):417–47.
- Sukumar N, Moran B, Belytschko T. The natural element method in solid mechanics. *Int J Numer Methods Eng*. 1998;43(5):839–87.
- Zhou ST, Liu YH, Chen SS. Upper bound limit analysis of plates utilizing the C^1 natural element method. *Comput Mech*. 2012;50(5):543–61.
- Zhou ST, Ma BJ, Hou CT, Tong J, Ju YT, Liu YH. C^1 natural element method for the plastic limit analysis of thin plates. *J Tsinghua Univ (Sci Technol)*. 2021;61(6):626–35 (in Chinese).
- Chen JS, Wu CT, Yoon S, You Y. A stabilized conforming nodal integration for Galerkin mesh-free methods. *Int J Numer Methods Eng*. 2001;50(2):435–66.
- Zhou ST, Liu YH, Wang DD, Wang K, Yu SY. Upper bound shakedown analysis with the nodal natural element method. *Comput Mech*. 2014;54(5):1111–28.
- Yoo JW, Moran B, Chen JS. Stabilized conforming nodal integration in the natural-element method. *Int J Numer Methods Eng*. 2004;60:861–90.
- Wang DD, Chen JS. A Hermite reproducing kernel approximation for thin plate analysis with sub-domain stabilized conforming integration. *Int J Numer Methods Eng*. 2008;74(3):368–90.
- Zhou ST. Investigations of dynamics for rotor structure and plasticity for plate structure. Beijing: Tsinghua University; 2014. (in Chinese).
- Zhou ST, Liu YH, Chen SS. Upper-bound limit analysis method of thin plates based on the nonconforming rectangular bending element. *J Tsinghua Univ (Sci Technol)*. 2011;51(12):1887–93 (in Chinese).
- König JA. Shakedown of elastic-plastic structures. Amsterdam: Elsevier; 1987.
- Wang XC. Finite element method. Beijing: Tsinghua University Press; 2003. (in Chinese).
- Shi DY, Mao SP, Chen SC. On the anisotropic accuracy analysis of ACM's nonconforming finite element. *J Comput Math*. 2005;23(6):635–46.

Springer Nature or its licensor (e.g. a society or other partner) holds exclusive rights to this article under a publishing agreement with the author(s) or other rightsholder(s); author self-archiving of the accepted manuscript version of this article is solely governed by the terms of such publishing agreement and applicable law.